STATIONKEEPING IN EARTH-MOON NEAR RECTILINEAR HALO ORBITS

Vivek Muralidharan[*] and Kathleen C. Howell[†]

Near Rectilinear Halo Orbits (NRHOs) are stable or nearly stable orbits that are defined as part of the L1 and L2 halo orbit families in the circular restricted three-body problem. Within the Earth-Moon regime, the L2 NRHOs offer candidate trajectories for the upcoming Gateway mission. The spacecraft, however, incurs continuous deviations due to unmodeled forces and orbit determination errors in this dynamically sensitive region. The current investigation focuses on a technique to maintain the spacecraft near a virtual reference orbit despite these uncertainties. For the stationkeeping scheme, flow dynamics in the region are utilized to categorically identify appropriate maneuver and target locations. The investigation reflects the impact of various factors on maneuver cost and efficacy. Additional feedback control is applied for phasing constraints.

INTRODUCTION

Lunar missions continue to generate serious interest among various space organizations across the globe. For example, with ever increasing research in the field of space physics, investigation of the celestial body nearest to Earth, i.e., the Moon, offers significant potential for scientific discoveries. In addition, with a focus on expanding the human presence in the region, NASA's Gateway mission, formerly the Deep Space Gateway (DSG) or Lunar Orbital Platform-Gateway (LOP-G) mission, delivers a hub-like facility that is currently planned to move along a Near Rectilinear Halo Orbit (NRHO) in the lunar vicinity.[1,2] Near rectilinear halo orbits are members of the halo orbit family in the L1 and L2 regions in the Earth-Moon circular restricted three-body problem.[3,4] These NRHOs are stable or nearly stable as characterized by the linear variational flow. Due to stability characteristics, NRHOs offer candidate orbits suitable for LOP-G as perturbations are expected to be manageable.

Motion along an NRHO is characterized by a reasonably close lunar passage and a large out-of-plane amplitude relative to the Earth-Moon orbit plane. The close passage to the Moon offers an opportunity to examine the Moon's polar region. In addition, spacecraft along some NRHOs offer a nearly uninterrupted link for relay communications to various landing sites for planned lunar landing missions.[5,6] In the higher-fidelity ephemeris model, the orbits are no longer closed, but quasi-periodic. With additional forces, the dynamics in the vicinity of the NRHO are more complex. The current investigation examines a stationkeeping scheme that effectively overcomes unmodeled errors as well as position and velocity uncertainty in orbit determination.

Stable orbits do not offer well-distinguished stable and unstable manifolds to be leveraged for stationkeeping, in contrast to unstable orbits with distinct unstable, stable and oscillatory modes.[7] Any perturbations generally include components aligned in the unstable manifold directions resulting in perturbations that grow over time. There are existing strategies, e.g., Floquet mode approach,[8–10] that computes a maneuver to nullify the unstable components of the perturbations such that the spacecraft is maintained near a reference path for a specified duration. However, for stable orbits this approach is less suitable. An alternate strategy, one that is based on the near symmetry of orbits along the line joining the primary bodies, is widely employed for

stationkeeping in the halo orbit region, including the stable NRHOs.[4,11–14] The technique is commonly identified as an x-axis control strategy and factors including maneuver location, time duration between successive maneuvers as well as the target horizon time affect its performance. This investigation explores the effect of these three factors on orbit maintenance cost and boundedness of spacecraft near the desired path.

BACKGROUND: NEAR RECTILINEAR HALO ORBITS

The circular restricted three-body problem (CR3BP) is a time invariant approximation for the spacecraft motion influenced by concurrent gravitational forces due to two primary bodies, e.g., the Earth and the Moon, rotating in circular orbits about their mutual barycenter.[15] The spacecraft is assumed to be infinitesimally small in mass such that it does not affect the motion of the Earth and the Moon. Consider a coordinate system, $\mathbb{R}$, rotating at a fixed rate, consistent with the revolution of the primary bodies, and defined by the dextral orthonormal triad $\hat{x}$, $\hat{y}$ and $\hat{z}$ to describe the motion of the spacecraft. The line joining the primaries, i.e., the Earth-Moon line represents the $\hat{x}$ axis in the rotating frame; the positive direction is a view from the Earth to the Moon. The $\hat{z}$ direction, is aligned in the direction normal to the Earth-Moon orbit plane. Finally, $\hat{y}$ completes the dextral coordinate system. The three spacial directions reflect the nonlinear spacecraft motion such that the position vector is represented as $\bar{r} = [x, y, z]^{\mathrm{T}}$ and velocity states by $\bar{v} = [\dot{x}, \dot{y}, \dot{z}]^{\mathrm{T}}$. Generally the 6-dimensional state is written by $\bar{\mathbf{x}} = [\bar{r}^{\mathrm{T}}, \bar{v}^{\mathrm{T}}]^{\mathrm{T}} = [x, y, z, \dot{x}, \dot{y}, \dot{z}]^{\mathrm{T}}$, where superscript 'T' implies transpose. Note that overbars represent vector quantities. Although the trajectories in the CR3BP serve as an approximation for the motion of the spacecraft, the CR3BP facilitates understanding of the underlying nonlinear dynamics. The CR3BP dynamics yield five equilibrium points, also labelled the libration points, or Lagrange points, denoted by L1 through L5, of which, L1, L2 and L3 are collinear to the line joining the primary bodies. The point L1 lies on the $\hat{x}$-axis between the primaries; L2 is on the far side of the Moon.

An infinite number of periodic orbits exist in the CR3BP as limit cycles. Such periodic solutions are explored as baseline trajectories for various mission scenarios. The location, stability properties and accessibility of these orbits are leveraged to satisfy requirements. Halo orbits are a type of family of periodic trajectories that exist near the collinear libration points in the circular restricted three-body problem.[16] Within the Earth-Moon system, the L1 and L2 halo orbits are being explored as potential destinations for a facility in cislunar space. Specifically for the Gateway mission, a southern L2 halo orbit is the current option. Some members of the L2 halo family with close approaches to the Moon and with high out-of-plane amplitudes are stable or nearly stable based on variational linear stability analysis.[3] Define the stability index to measure the stability characteristics of a periodic orbit such that $\nu = 1/2(\lambda_i + 1/\lambda_i)$, where λ_i are the non-unity eigenvalues from the monodromy matrix, i.e., the state transition matrix over precisely one orbital period. For stable orbits, the stability index $|\nu| \leq 1$. The stable or nearly stable orbits in the halo orbit family are characterized as the Near Rectilinear Halo Orbits (NRHO). The family of L2 southern halo orbits in the Earth-Moon system is plotted in Figure 1. The orbits colored in red are the NRHOs. In addition, the periods of the NRHOs range across a block of values such that some of these orbits exhibit different resonance properties. For the stationkeeping analysis, orbits are selected with different perilune radius distances including those that demonstrates simple resonance ratios.

HIGHER-FIDELITY MODEL

The higher-fidelity ephemeris model is a better approximation for the spacecraft motion but generally exhibits characteristics similar to the motion predicted by the CR3BP. Using the N-body relative equations of motion, a more accurate representation of the spacecraft motion is rendered, one that accommodates the time-varying relative location of the celestial bodies in modeling the gravitational
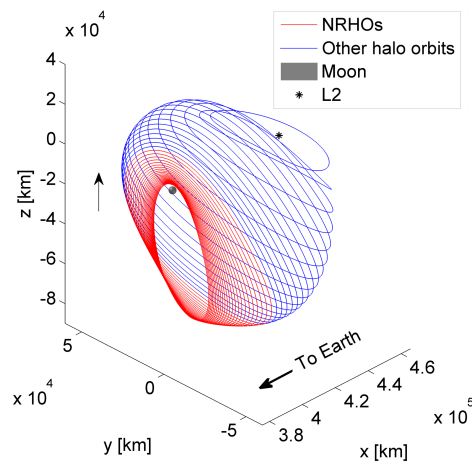

Figure 1: Earth-Moon L2 southern halo orbits

forces acting on the spacecraft. NASA's Jet Propulsion Laboratory (JPL) offers a package for numerical approximations of the relative locations of celestial bodies in terms of SPICE Kernels.[17] Not surprisingly, the CR3BP position and velocity states, when propagated in the ephemeris model using SPICE data, deviate from the path predicted by the CR3BP model. To generate a continuous natural trajectory in the higher-fidelity model, multiple revolutions of the CR3BP orbit are stacked and corrected using a multiple shooting algorithm for position and velocity continuity.[18] The iterative procedure produces a quasi-periodic trajectory in the higher-fidelity model that resembles the geometry of the corresponding orbit defined in the CR3BP. The L2 southern NRHO with perilune radius 3200 km in the ephemeris model is plotted in Figure 2, in three different views, the rotating frame of view, $\mathbb{R}$, the Moon-centered inertial view as well as the Earth-centered inertial view. The natural trajectory in the ephemeris model offers a virtual reference solution that serves as an anchor for stationkeeping operations; the virtual reference is updated over time as appropriate. The fidelity of the model is enhanced by adding the effect of a large number of celestial bodies but too many additional bodies is computationally intensive and may be nontrivial, when incorporating additional orbit determination errors. Based on other investigations,[19] the gravitational forces due to the Earth, Moon and the Sun, and the Solar Radiation Pressure (SRP), are the most dominant forces on the Earth-Moon halo orbits in the L1 and L2 region, and sufficient for this analysis. The effect of any additional forces are minimal, however, for comparison with other stationkeeping literature, gravitational force due to Jupiter is also included.[4,11] Ephemeris data is incorporated using the DE421 model.

X-AXIS CONTROL STATIONKEEPING SCHEME

Any type of spacecraft mission requires regular orbit maintenance operations for long-term sustainability. The orbits are subject to sensitive dynamics that perturb spacecraft from the desired path. In this investigation, stationkeeping operations maintain the spacecraft in the vicinity of a long horizon virtual reference solution that is generated incorporating science constraints and phase constraints such as eclipse avoidance.[4,11] The virtual reference is updated over time as appropriate. Several stationkeeping techniques are evaluated on the Earth-Moon L1 and L2 orbits, i.e., Lyapunov and halo orbits, both stable and unstable.[4,11,13,14,18–21] Since the Gateway mission is planned for launch in the early 2020s and is expected to operate in the 9:2 synodic resonant NRHO, with a radius of periapsis approximately 3200 km from the Moon, it serves as a baseline trajectory to test the efficiency of a control strategy
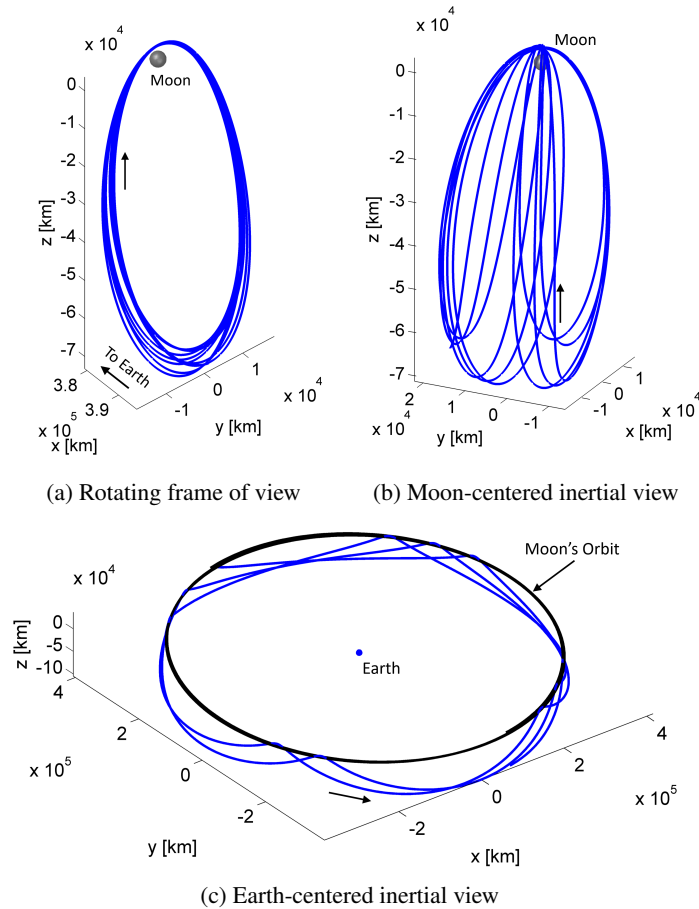

(a) Rotating frame of view   (b) Moon-centered inertial view

(c) Earth-centered inertial view

Figure 2: L2 NRHO with perilune radius 3200 km in higher-fidelity ephemeris model.

3

for stationkeeping on NRHOs. Of course, the control strategy must also be applicable to other low perilune radius NRHOs. This investigation focuses on leveraging the underlying dynamics to improve the control algorithm and parameter selection process.

Recent analyses have focused on the x-axis control algorithm for successful missions[14, 21] and is currently employed for analysis on the Gateway mission.[4, 11, 22] The x-axis control strategy generally relies on the symmetry of the NRHOs across the xz plane in the rotating frame of reference. In the CR3BP model, the rotating $\dot{x}$ value along the orbit at the xz plane crossing is zero. The notion of a zero value for the rotating $\dot{x}$ velocity component at the xz plane crossing is exploited for orbit maintenance operations. Due to complex dynamics in the higher-fidelity ephemeris model, the natural trajectory that resembles the NRHO does not possess a precise value of $\dot{x} = 0$ at the xz plane crossing, hence, it is further constrained that the rotating $\dot{x}$ value along the actual trajectory matches the $\dot{x}$ value along a long horizon virtual reference path at the xz plane crossing, within an acceptable tolerance.

The stationkeeping operation is a sequential process. A baseline trajectory is introduced that acts as a long horizon virtual reference solution. From previous invesigations,[4, 11] it is seen that targeting xz plane crossings near the periapsis region yields low stationkeeping costs. Since the periapsis region of the NRHO is particularly sensitive to perturbations, delivering an accurate maneuver that reduces deviations in the rotating $\dot{x}$ value at the xz plane crossings near the periapsis is worth exploring for long-term low-cost maintenance. The algorithm also targets the rotating $\dot{x}$ value at subsequent xz plane crossings along the evolving path. The $\dot{x}$ values at each of the xz plane crossings near the periapsis on the long horizon virtual reference solution are recorded. The spacecraft state is originally introduced at the halo orbit injection epoch with additional white noise in both position and velocity states, and with specified mean and variance. In the ephemeris model, additional uncertainty in solar radiation pressure is introduced with errors in the coefficient of reflection C_r and the surface area of the spacecraft model. The perturbed states are propagated to a predetermined maneuver location, generally closer to the apoapsis region, and a maneuver $\Delta \bar{v}$ is computed to meet the goal of achieving the $\dot{x}$ value along the virtual baseline at a specified downstream xz plane crossing, within some predefined tolerance, considered as 0.45 m/s is this investigation.[4] The target xz plane crossing may be the 1st, 2nd, ..., n^{th} crossing, increasing further downstream along the propagated trajectory. If the targeting process fails to compute a successful maneuver that meets the goal for a specified target, the target horizon time is reduced and the process is simulated again until a successful maneuver is computed. Additional white noise modelled as maneuver execution error is incorporated into the maneuver and implemented. Along the subsequent path, the states are updated and further perturbed with navigational errors and solar radiation pressure errors and the procedure is continued till the end of the mission duration. In contrast, if none of the target horizon times delivers a successful maneuver, the particular simulation is considered as failed. The total sum of the maneuvers $|\Delta \bar{v}|$ over each run is recorded. Since white noise is generated randomly, a Monte Carlo simulation is performed over 100 runs and the mean cost is estimated.[18] With 100 samples, the standard error of the mean is reduced to 10% of the sample standard deviation.[10, 23] The total cost is then linearly extrapolated over one year to estimate an annual maintenance cost.

Orbit determination and model error

Spacecraft experience multiple perturbations due to unmodeled forces and limitations on orbit determination. To simulate these perturbing conditions, different error levels in the orbit determination process and modeling formulations are introduced. The spacecraft is intentionally perturbed from the reference trajectory to simulate a stationkeeping operation. Two different navigation error levels are considered, a low orbit determination error (ODE) level with mean 0 and standard deviation (3σ) of 1 km in position magnitude and 1 cm/s in velocity magnitude, and a relatively high orbit determination error (ODE) level with mean 0 and standard deviation (3σ) of 10 km in position magnitude and 10 cm/s in velocity magnitude. Consistent with the navigation error, the same error levels are used for orbit insertion. Further, maneuver execution error is introduced as a fixed error with a perturbation of 0.03 cm/s in any arbitrary direction.

Solar radiation pressure (SRP) is introduced into the model to simulate the spacecraft motion, however, the exact orientation of the spacecraft is unknown, hence SRP errors are introduced to simulate the perturbing force. A cannonball model for the spacecraft is assumed with mass 25848 kg, projected area of 50 sq.m. and

a perfectly reflective surface with coefficient of reflectivity $C_r = 2$.[4,12] Uncertainty (1σ) in the projected area is assumed to be 5% and uncertainty in C_r to be 10% for all simulations.

Stationkeeping parameters

The stationkeeping algorithm depends on various parameters that influence the annual cost and the boundedness of a spacecraft trajectory near a virtual reference solution. The stationkeeping parameters that are user-defined impact its performance. For orbit maintenance using the x-axis control approach, three factors that impact the overall cost and the deviation from the reference path are explored in this investigation:

- Coast duration
  Currently, the stationkeeping process is based on impulsive maneuvers and, hence, between two successive maneuvers the spacecraft coasts under the natural dynamics. The minimum time duration between two successive maneuvers is defined as the coast duration. It is generally expected that, for a stable orbit, maneuvers with wider spacing are effective in reducing costs, in contrast to an unstable orbit that may require maneuvers spaced relatively close for effective orbit maintenance. In addition, NRHOs frequently possess close lunar passages, a nonlinear effect that influences the dynamical flow near the reference orbit over time.

- Maneuver location
  Not all locations around the orbit offer the same characteristic properties. Some locations are notably more sensitive depending on the proximity to different gravitational bodies. These sensitive locations may offer maximum benefits if stationkeeping maneuvers are implemented accurately.[24] However, the primary function of a stationkeeping maneuver is to overcome error build-ups due to limitations in the orbit determination process and errors due to prior maneuvers. These sensitive locations often increase the measurement uncertainty, therefore, precise maneuvers are impossible in practice. These drawbacks, coupled with errors in maneuver execution, result in these sensitive regions being inferior maneuver locations as errors in the sensitive regions amplify rapidly over time.

- Target horizon
  The length of time between the maneuver location and the targeted xz plane crossing near the periapsis region is denoted the target horizon. Since the target horizon is user defined, the target is placed at the first xz plane crossing near the periapsis, or the second crossing near the next periapsis or so on. Since the target location is an xz plane crossing, the target horizon is labelled in terms of the number of revolutions downstream from the maneuver location. A precise maneuver is generated by targeting the rotating $\hat{x}$ value at the specified xz plane crossing. Because of the error-free maneuvers generated in a single shooting process, it is generally reliable to target a sensitive region, e.g., the periapsis region, to yield the most economic maneuver. Guzzetti et al. suggest the same principle based on their results by targeting the xz plane crossings near the periapsis.[4] A longer target horizon, i.e., targeting further downstream, is expected to produce lower maneuver magnitudes, however, mission requirements or constraints may necessitate shorter target horizons.

The inter-dependency of the parameters, i.e., coast duration, maneuver location and target horizon, is illustrated in the flowchart in Figure 3. The simultaneous interactions between the flow evolving from one maneuver location to the next along a coast arc, and the flow evolution from the maneuver location to the target, determines the performance of the maneuver.

Effect of maneuver location and coast duration The spacecraft coasts under the natural dynamics between two successive impulsive maneuver locations, and the time interval is termed the coast duration. The flow between the maneuver locations then determines the impact of the deviations in the initial states that are propagated downstream to the end states where the subsequent maneuver is generated. The dynamics of the flow in the circular restricted three-body problem as well as in the ephemeris model are complex, however, for small perturbations in a linear model, predictions of the flow variations in the vicinity of a reference trajectory using the state transition matrix (STM) is generally reliable for these NRHOs. The Cauchy-Green tensor
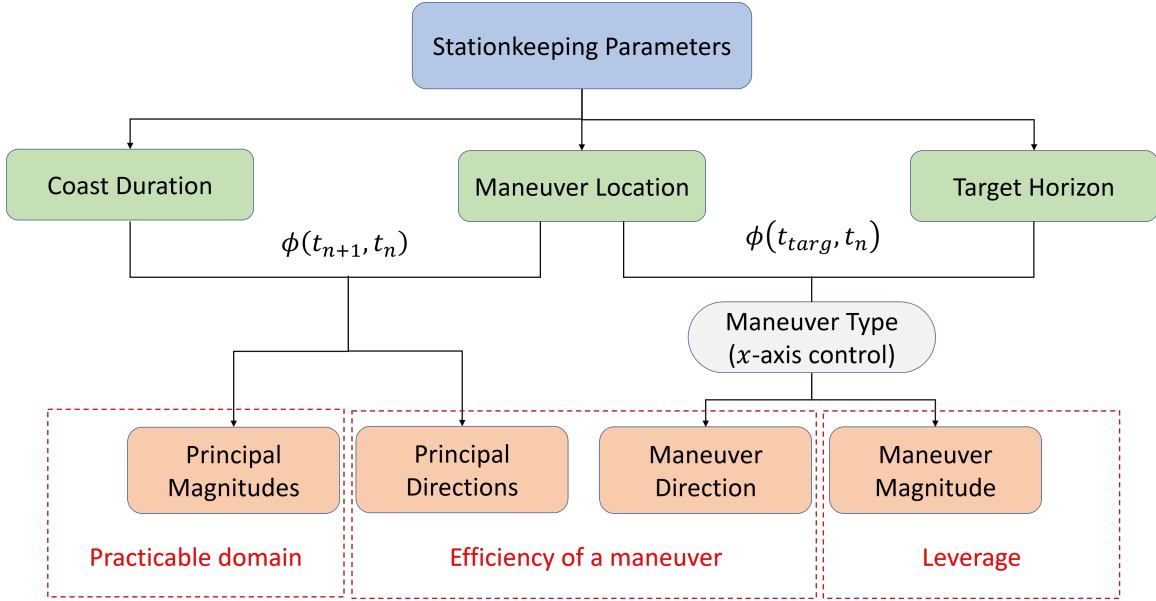
Figure 3: Stationkeeping parameter efficiency flowchart.

(CGT) is a function of the STM and aids in visualizing linear flow by decomposing it into different mutually orthogonal directions, along which components of perturbations grow independent of the other. Since maneuvers are allowed anywhere along the orbit (multiple maneuvers per orbit or multiple orbits between maneuvers) the mutual impact of maneuver location and coast duration is vital.

The Cauchy-Green tensor (CGT) is a function of the state transition matrix (STM) that yields valuable information concerning the linearized variational dynamical flow in the vicinity of a reference solution.[25, 26] While the STM, ϕ, relates the variation of each individual state over time such that $\phi(t, t_0) = \frac{\partial \bar{\mathbf{x}}(t)}{\partial \bar{\mathbf{x}}_0}$, the CGT relates the evolution of the perturbations represented as a material volume over time. The STM evaluated on a reference trajectory, $\bar{\mathbf{x}}^*(t)$, maps the initial perturbation, $\delta \bar{\mathbf{x}}_0$, to the final perturbed states, $\delta \bar{\mathbf{x}}_f$, as a linear correlation, i.e.,

$$\delta \bar{\mathbf{x}}_f = \phi(t_f, t_0)\delta \bar{\mathbf{x}}_0 \tag{1}$$

where, t_0 and t_f are the initial and final epochs. The isochronous perturbations are measured relative to this reference path as $\delta \bar{\mathbf{x}}(t) = \bar{\mathbf{x}}(t) - \bar{\mathbf{x}}^*(t)$. The CGT, or simply '$\mathbb{C}$' is evaluated as

$$\mathbb{C}(t_f, t_0) = \phi(t_f, t_0)^{\mathrm{T}}\phi(t_f, t_0) \tag{2}$$

and defines the deformation, as a product of the transpose (superscript T) of the state transition matrix, ϕ, with itself. Physically, CGT renders the square of the magnitude of the final deformation to the initial deformation as

$$||\delta \bar{\mathbf{x}}_f||^2 = \delta \bar{\mathbf{x}}_f^{\mathrm{T}}\delta \bar{\mathbf{x}}_f = \delta \bar{\mathbf{x}}_0^{\mathrm{T}}\phi(t_f, t_0)^{\mathrm{T}}\phi(t_f, t_0)\delta \bar{\mathbf{x}}_0 = \delta \bar{\mathbf{x}}_0^{\mathrm{T}}\mathbb{C}(t_f, t_0)\delta \bar{\mathbf{x}}_0. \tag{3}$$

The growth or decay of the quantity $||\delta \bar{\mathbf{x}}_f||^2$ describes the sensitivity of the trajectory to the initial perturbation, $\delta \bar{\mathbf{x}}_0$, however, when the size of an initial perturbation is undefined, the sensitivity information is directly extracted from CGT. The eigen-decomposition of the CGT, or the singular value decomposition of the STM, yields details about directions and magnitudes of the stretching.

The flow reflecting the impact of the perturbation and emulated by a material volume is characterized primarily by the magnitudes and directions of the elongation. The flow for any volume is visualized either using the eigen-decomposition or the singular value decomposition of the corresponding matrices. The eigen-decomposition of the CGT yields the eigenvalues λ_i and the eigen-vectors $\mathbb{V}_i$. For a linear system, the contraction or expansion of the local phase space is captured by σ_i in the directions in $\mathbb{V}_i$. Note that $\sigma_i = $

6

$\sqrt{\lambda_i}$. The singular value decomposition (SVD) of the STM, reveals the same critical details about the flow in the phase space but with an additional directional information, $\mathbb{U}_i$. Mathematically, the STM is decomposed into the matrices, $\mathbb{U}$, Σ and $\mathbb{V}$, such that,

$$\mathbb{U}\Sigma\mathbb{V}^* = \phi(t_f, t_0) \tag{4}$$

where, the columns of $\mathbb{U}$ yield the stretching directions at the final epoch. For a square matrix, ϕ, Σ is a diagonal matrix with the magnitude of the stretching along different directions in descending order, i.e., $\sigma_1 > \sigma_2 > \ldots > \sigma_n$, such that $\sigma_i = \Sigma_{ii}$, an element in Σ in the ith row and i^{th} column. The matrix $\mathbb{V}$ then provides the principal stretching directions at the initial time along the propagated arc. The matrices Σ and $\mathbb{V}$ essentially supply the same details, acquired using an eigenvalue decomposition of $\mathbb{C}$, while $\mathbb{U}$ offers additional information captured using singular value decomposition, also derivable from the Cauchy-Green tensor. The matrices $\mathbb{U}$ and $\mathbb{V}$ are each orthogonal. Figure 4 illustrates the contraction or expansion along different flow directions with the example of a two-dimensional system transitioned through CGT. Consider a unit circle in the phase space near an initial reference path that undergoes deformation and evolves into a stretched ellipse. The evolution of this unit circle into an ellipse is a combination of translation and rotation. The matrices $\mathbb{U}$ and $\mathbb{V}$ supply the rotation information while the matrix Σ yields information concerning linear

Figure 4: Principal stretching directions.

translation. The columns of the matrix $\mathbb{V}$ represented by $\mathbb{V}_i$ indicate the principal directions at the initial time that evolve into $\mathbb{U}_i$ (the columns of matrix $\mathbb{U}$). The diagonal elements of the matrix Σ, or σ_i, indicate the stretching along corresponding principal directions.
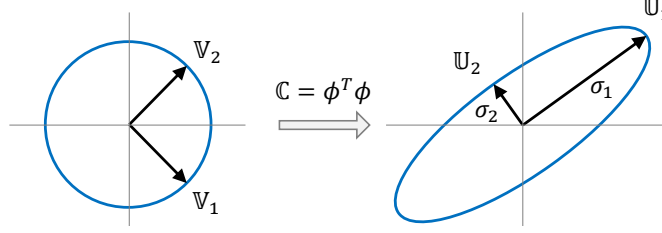
A maneuver is deliverable anywhere along a range of locations on the orbit, hence, identifying precise maneuver locations is vital for the analysis. Maneuver locations and trajectory segment lengths are, thus, denoted in terms of a mean anomaly and an osculating true anomaly. Since the NRHO is a closed orbit in the CR3BP, the mean anomaly is defined as $\theta_{MA} = 2\pi\ t/T\ rad = 360\ t/T\ deg$ where T is the time period for the selected orbit while t is the time of propagation beyond the most recent periapsis as defined in the circular restricted three-body problem. Since the NRHO is not a Keplerian orbit, an osculating true anomaly, θ_{TA}, is defined with respect to a central body, the Moon.[27] The mean anomaly quantifies the relative locations in terms of the actual time of propagation while true anomaly offers the geometric interpretation of locations as noted in Figure 5.

The flow between the nth and $(n+1)^{\text{th}}$ impulsive maneuvers, at time t_n and t_{n+1} respectively, is measured by the state transition matrix evaluated along the coast segment, i.e., φ_C, such that $\varphi_C = \phi(t_{n+1}, t_n)$. Without loss of generality, assume, $t_n = t_0$, as the initial time at which the maneuver is implemented, and $t_{n+1} = t_f$, as the final time along the propagated natural trajectory segment. Consider

$$\varphi_C(t_f, t_0) = \begin{bmatrix} \varphi_{C,r,r} & \varphi_{C,r,v} \\ \varphi_{C,v,r} & \varphi_{C,v,v} \end{bmatrix} = \begin{bmatrix} \frac{\partial \bar{r}_f}{\partial \bar{r}_0} & \frac{\partial \bar{r}_f}{\partial \bar{v}_0} \\ \frac{\partial \bar{v}_f}{\partial \bar{r}_0} & \frac{\partial \bar{v}_f}{\partial \bar{v}_0} \end{bmatrix} \tag{5}$$

where $\varphi_{C,r,r}$, $\varphi_{C,r,v}$, $\varphi_{C,v,r}$ and $\varphi_{C,v,v}$ are the 3×3 submatrices of 6×6 matrix φ_C. In the stationkeeping problem, however, only the initial velocity terms are controllable, hence tracking the flow generated by the 6×6 state transition matrix φ_C is inconsequential. Specific submatrices of φ_C yield more relevant characteristics. For example, the 3×3 dimensional submatrix, $\varphi_{C,r,v}$, maps the initial velocity perturbation, $\delta\bar{v}_0$, to the final position change, $\delta\bar{r}_f$, and the 3×3 dimensional submatrix, $\varphi_{C,v,v}$, maps the initial velocity perturbation, $\delta\bar{v}_0$, to the final velocity change, $\delta\bar{v}_f$. Also, combined, the 6×3 dimensional submatrix $\varphi_{C,rv,v}$, where

$$\varphi_{C,rv,v} = \begin{bmatrix} \varphi_{C,r,v} \\ \varphi_{C,v,v} \end{bmatrix} \tag{6}$$

7

that maps the initial velocity perturbation, $\delta\bar{v}_0$, to the final position and velocity state change, $\delta\bar{r}_f$ and $\delta\bar{v}_f$, yields significant characteristics, as only the initial velocity states, $\delta\bar{v}_0$, are subject to change. The sensitivity of the orbit states to initial velocity changes is measured by monitoring the magnitude of maximum stretching, σ_1, corresponding to each of the $\varphi_{C,r,v}$, $\varphi_{C,v,v}$ and $\varphi_{C,rv,v}$ submatrices. The values of the largest stretching magnitudes, σ_1, corresponding to each of the $\varphi_{C,r,v}$, $\varphi_{C,v,v}$ and $\varphi_{C,rv,v}$ submatrices for various combinations of maneuver locations and coast durations along the 9:2 synodic resonant orbit with perilune radius 3200 km is plotted in Figure 6. Not surprisingly, the maximum
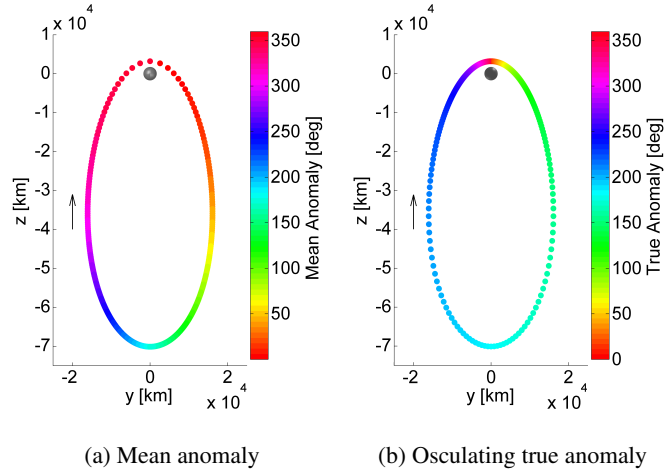

(a) Mean anomaly   (b) Osculating true anomaly

Figure 5: Definition of orbit locations (L2 NRHO with 3200 km perilune radius).

stretching magnitudes corresponding to $\varphi_{C,v,v}$ and $\varphi_{C,rv,v}$, the submatrices that include velocity perturbations at the final time, are significantly larger, suggesting that the velocity changes generally must be tightly controlled. Due to such behavior, flow described by the $\varphi_{C,v,v}$ and $\varphi_{C,rv,v}$ submatrices offer measurements to identify sensitive regions along the orbit. Since the stationkeeping algorithm is required to reduce the successive maneuver magnitudes, the stretching direction from the $\varphi_{C,v,v}$ submatrix, that monitors the final velocity change, is incorporated throughout this investigation. Further, as is evident from Figure 6, trajectory segments that terminate close to or originate near the periapsis regions are highly sensitive to perturbations, i.e., hotter shades in the map, hence, maneuvers are generally avoided in such regions. The cooler shades in the map, highlight the likely regions suitable for selecting the maneuver locations.

Effect of maneuver location and target horizon The flow between the maneuver location and the target determines the maneuver characteristics. As previously introduced, for an x-axis control strategy, the rotating $\dot{x}$ value at different xz plane crossings near the periapsis region serves as a target parameter. The stationkeeping control effort is represented by

$$\Delta\dot{x}_f = \begin{bmatrix} \varphi_{T,44} & \varphi_{T,45} & \varphi_{T,46} \end{bmatrix} \Delta\bar{v}_0 \tag{7}$$

where, $\Delta\dot{x}_f$ is the change in the rotational $\dot{x}$ value at the target and $\Delta\bar{v}_0 = [\Delta\dot{x}_0, \ \Delta\dot{y}_0, \ \Delta\dot{z}_0]^{\mathrm{T}}$ defines a column vector with three scalar independent control variables that comprise the impulsive maneuver. Finally, $[\varphi_{T,44} \ \varphi_{T,45} \ \varphi_{T,46}]$ is the appropriate submatrix of the state transition matrix, φ_T. The subscripts, i and j, in $\varphi_{T,ij}$, indicate the element in φ_T in the ith row and j^{th} column. Moreover, φ_T is the state transition matrix from the maneuver location to the target, i.e., $\varphi_T = \phi(t_{Target}, t_0)$. The time difference between t_0 and t_{Target} is the target horizon time. Define $\bar{M} = [\varphi_{T,44} \ \varphi_{T,45} \ \varphi_{T,46}]^{\mathrm{T}}$ as a 3×1 column vector and, therefore, $\Delta\dot{x}_f = \bar{M}^{\mathrm{T}}\Delta\bar{v}_0$. The goal for the stationkeeping process is minimizing the propellant costs, hence, a minimum norm solution that delivers the smallest maneuver is generally an appropriate choice for this problem. Since the control equation $\Delta\dot{x}_f = \bar{M}^{\mathrm{T}}\Delta\bar{v}_0$ is equivalent to the dot product between $\bar{M}$ and the $\Delta\bar{v}_0$ vector, the maneuver magnitude is deduced as

$$|\Delta\dot{x}_f| = |\bar{M}||\Delta\bar{v}_0| \cos\vartheta \ \longrightarrow \ |\Delta\bar{v}_0| = \frac{|\Delta\dot{x}_f|}{|\bar{M}| \cos\vartheta} \tag{8}$$

where $\cos\vartheta$ is the angle between $\bar{M}$ and the $\Delta\bar{v}_0$ vector. Of course, $\bar{M}$ includes components of the state transition matrix φ_T but $\Delta\bar{v}_0$ and ϑ are variables. In any case, the smallest maneuver $|\Delta\bar{v}_0|$ is generated only if $\cos\vartheta = 1$, i.e., $\vartheta = 0^o$ or $\Delta\bar{v}_0$ vector is aligned in the direction of $\bar{M}$. Therefore, a minimum norm solution for stationkeeping renders a maneuver magnitude of

$$|\Delta\bar{v}_0|_{min-norm} = \frac{|\Delta\dot{x}_f|}{|\bar{M}|} \tag{9}$$

8

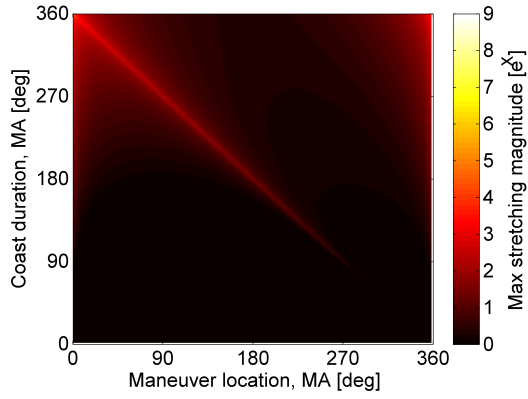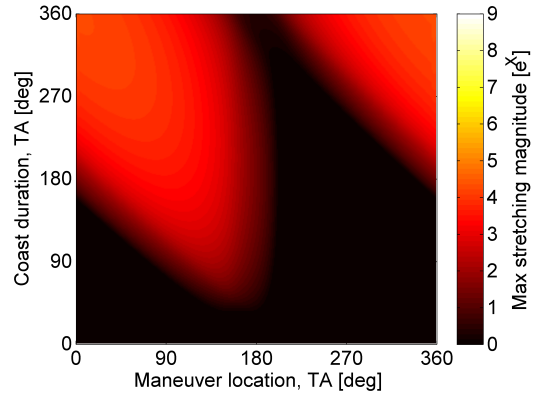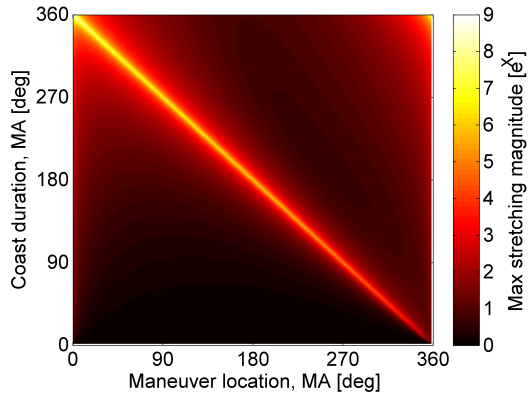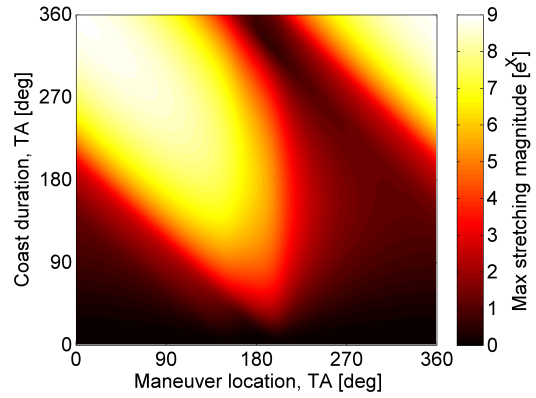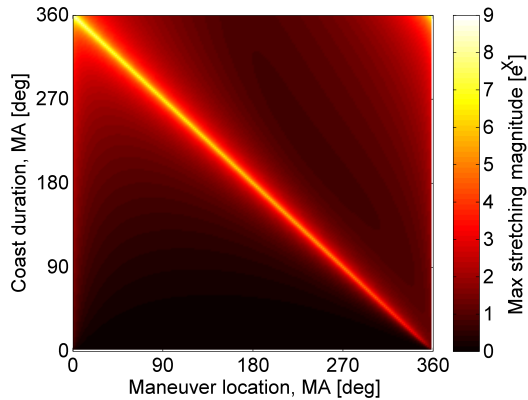(a) Maximum stretching of $\varphi_{C,r,v}$ for measurements in mean anomaly

(b) Maximum stretching of $\varphi_{C,r,v}$ for measurements in true anomaly
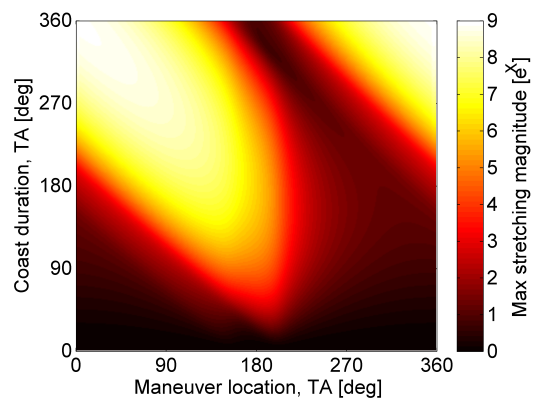
(c) Maximum stretching of $\varphi_{C,v,v}$ for measurements in mean anomaly

(d) Maximum stretching of $\varphi_{C,v,v}$ for measurements in true anomaly

(e) Maximum stretching of $\varphi_{C,rv,v}$ for measurements in mean anomaly

(f) Maximum stretching of $\varphi_{C,rv,v}$ for measurements in true anomaly

Figure 6: Maximum stretching magnitudes for different submatrices of the state transition matrix along the NRHO with a perilune radius of 3200 km.

in the direction of $\bar{M}$. The maneuver magnitude that is generated depends on the change in rotational velocity $\Delta\dot{x}_f$, one that varies with time, however, the maneuver magnitude as a function of the initial perturbation is a better metric, i.e.,

$$|\Delta\bar{v}_0|_{min-norm} = \frac{|\bar{B}^{\mathrm{T}}\Delta\bar{\mathbf{x}}_0|}{|\bar{M}|} \leq \frac{|\bar{B}^{\mathrm{T}}||\Delta\bar{\mathbf{x}}_0|}{|\bar{M}|} \tag{10}$$

where $\Delta\dot{x}_f = \bar{B}^{\mathrm{T}}\Delta\bar{\mathbf{x}}_0$ with $\bar{B} = [\varphi_{T,41}\ \varphi_{T,42}\ \varphi_{T,43}\ \varphi_{T,44}\ \varphi_{T,45}\ \varphi_{T,46}]^{\mathrm{T}}$ as the submatrix of φ_T that relates the initial state perturbation that delivers a final $\dot{x}$ change. The initial perturbed state is defined as $\Delta\bar{\mathbf{x}}_0 = [\Delta x_0,\ \Delta y_0,\ \Delta z_0\ \Delta\dot{x}_0,\ \Delta\dot{y}_0,\ \Delta\dot{z}_0]^{\mathrm{T}}$. The inequality in equation (10), represented in the standardized form as

$$\frac{|\Delta\bar{v}_0|_{min-norm}}{|\Delta\bar{\mathbf{x}}_0|} \leq \frac{|\bar{B}|}{|\bar{M}|} \tag{11}$$

expresses the influence of different target horizons on the stationkeeping maneuver. A plot of $\frac{|\bar{B}|}{|\bar{M}|}$ for different targets, i.e., 1st, 2nd and 7th xz plane crossings near the periapsis region is represented in Figure 7 for an L2 NRHO with perilune radius 3200 km. For different target horizons, maneuver locations along the orbit offer distinct characteristics. A lower value of $\frac{|\bar{B}|}{|\bar{M}|}$ suggests that the maneuver executed produces a smaller magnitude in that region. From Figures 7(e) and 7(f), it is evident that when targeting the 7th xz plane crossing, there exists a wide range of maneuver locations that result in low maneuver magnitudes compared to targeting the rotating $\dot{x}$ at the 1st or 2nd xz plane crossings as in Figures 7(a), 7(b), 7(c) and 7(d).

The ratio $\frac{|\bar{B}|}{|\bar{M}|}$ provides the upper limit on the value of the maneuver magnitude for a given magnitude of the initial perturbation, however, the direction of the maneuver is governed by the direction of the $\hat{M}$ vector. The direction of the maneuver is an important parameter that yields an assessment for the efficiency of the maneuver in maintaining the spacecraft in the vicinity of the reference path. The stretching directions for the submatrices of the STM along the coast segment, φ_C, are available; such a quantity offers insight for predicting a maneuver that likely results in the spacecraft deviating from the reference trajectory. Geometrically, if the maneuver direction $\hat{M}$ is aligned in the most stretching direction $\mathbb{V}_1$, with $\sigma_1 > 1$, then the executed maneuver produces the maximum change in the state at the following maneuver location thereby increasing the spacecraft deviation from the reference. In contrast, if the maneuver direction $\hat{M}$ is aligned perpendicular to the most stretching direction $\mathbb{V}_1$, the executed maneuver reduces the deviation at the following maneuver location. If the stretching along the directions associated with σ_2 and σ_3 are less than a nondimensional value of 1, then the plane represented by the $\mathbb{V}_2 - \mathbb{V}_3$ vectors defines a restoring plane. If, only $\sigma_3 < 1$, then the direction along the $\mathbb{V}_3$ vector is a restoring direction. The restoring plane or the restoring direction is vital as deviations at the end of the propagated arc diminish in comparison to deviations at the beginning. The maneuvers, when executed in the restoring plane or along the restoring direction, reduces the spacecraft deviation at the downstream locations, thereby maintaining the spacecraft boundedness. A map for the direction between the maneuver and the most stretching direction for different combination of maneuver location and coast duration for three different target horizons is presented in Figure 8, for an L2 NRHO with perilune radius 3200 km. Regions such that the maneuver and the most stretching direction are almost perpendicular facilitate efficient maneuvers.

Conventional approach

For orbit maintenance operations as simulated in the ephemeris model by Davis et al.[11] as well as Guzzetti et al.[4] for Earth-Moon L2 NRHOs, maneuvers are implemented once per revolution, generally at (or near) the apoapsis. Since the period of the NRHO is approximately one week, performing maneuvers only in the apoapsis region provides ample time for orbit determination. The annual stationkeeping costs estimated by targeting the rotating $\dot{x}$ value at the xz plane crossing 6.5 revolutions ahead produces the most economic result, for various orbit determination error levels, both in position and velocity. A similar trend is observed for simulations in the CR3BP model. The intuition that a longer target horizon consistently produces a lower maneuver cost, is not necessarily true for the L2 NRHOs, however. For the L2 NRHO with a radius of periapsis 3200 km, the target horizon at 1.5 revolutions results in several failed Monte Carlo cases or a high
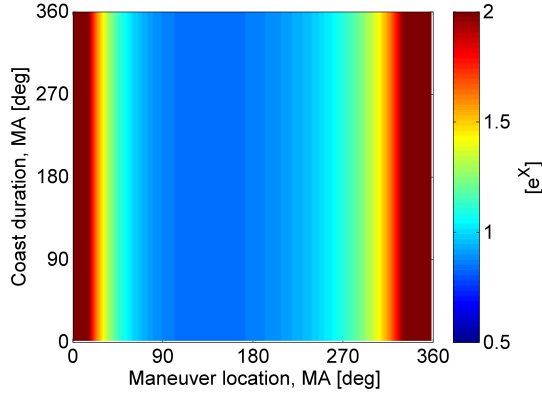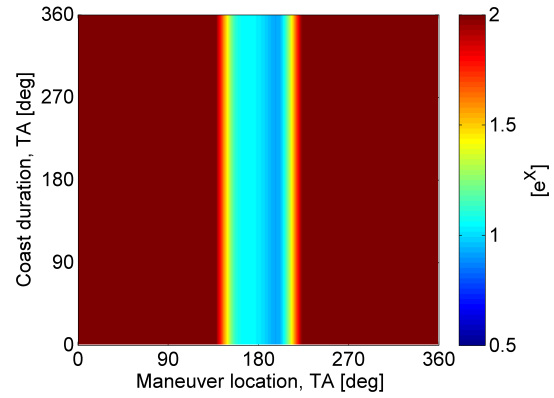
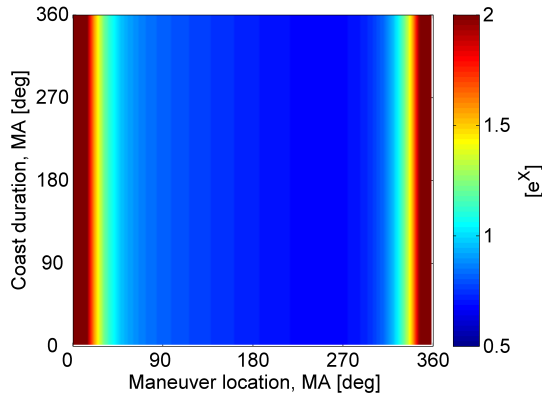(a) Target: 1st xz plane crossing near periapsis. Measurement: Mean anomaly.
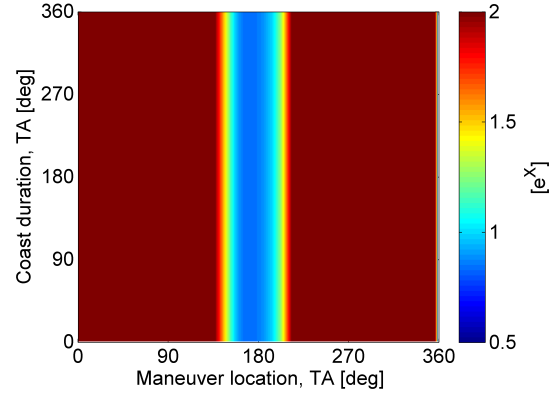
(b) Target: 1st xz plane crossing near periapsis. Measurement: Osculating true anomaly.
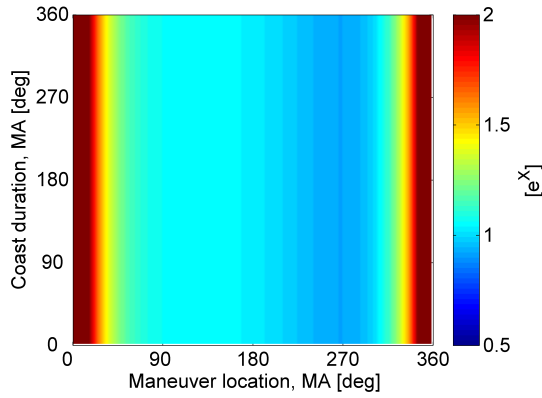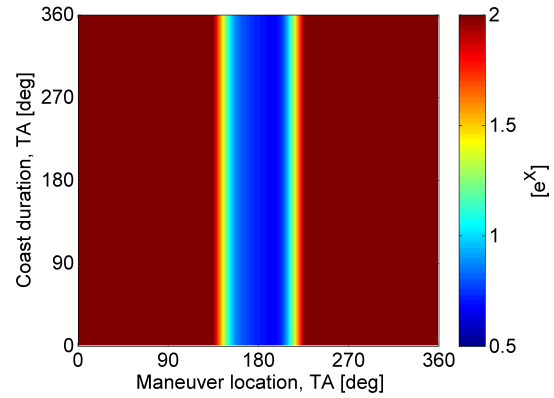
(c) Target: 2nd xz plane crossing near periapsis. Measurement: Mean anomaly.

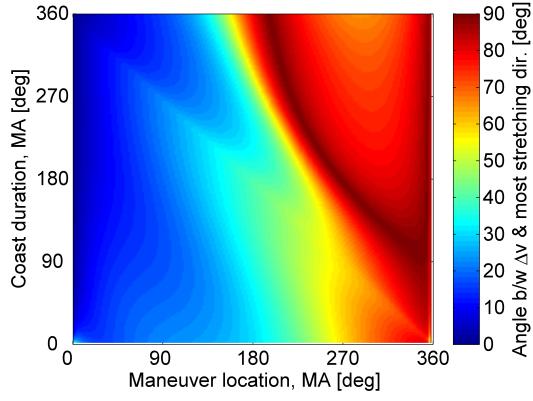(d) Target: 2nd xz plane crossing near periapsis. Measurement: Osculating true anomaly.

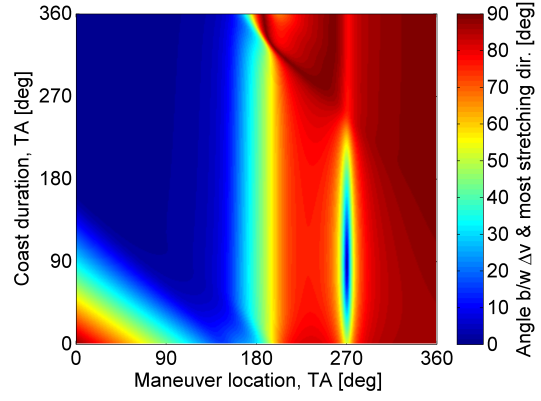(e) Target: 7th xz plane crossing near periapsis. Measurement: Mean anomaly.

(f) Target: 7th xz plane crossing near periapsis. Measurement: Osculating true anomaly.
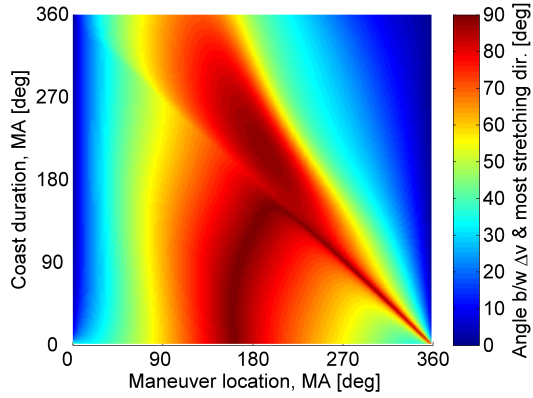
Figure 7: Ratio of maximum maneuver magnitude per magnitude of the initial state deviation, $\frac{|\bar{B}|}{|\bar{M}|}$, for different target horizons. Reference orbit: L2 NRHO with perilune radius 3200 km.
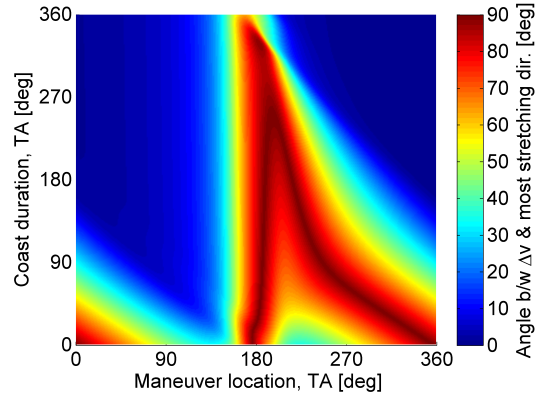
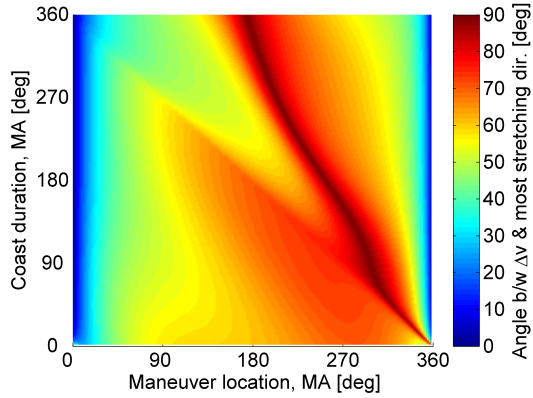(a) Target: 1st xz plane crossing near periapsis. Measurement: Mean anomaly.

(b) Target: 1st xz plane crossing near periapsis. Measurement: Osculating true anomaly.

(c) Target: 2nd xz plane crossing near periapsis. Measurement: Mean anomaly.

(d) Target: 2nd xz plane crossing near periapsis. Measurement: Osculating true anomaly.

(e) Target: 7th xz plane crossing near periapsis. Measurement: Mean anomaly.

(f) Target: 7th xz plane crossing near periapsis. Measurement: Osculating true anomaly.
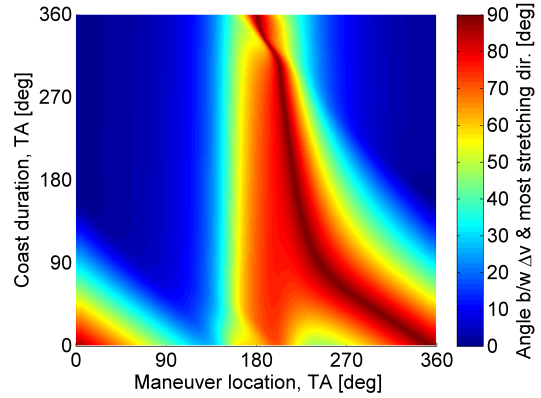
Figure 8: Estimated angle between maneuver direction and most stretching direction $\mathbb{V}_1(\varphi_{C,v,v})$ for different target horizons. Reference orbit: L2 NRHO with perilune radius 3200 km.

maintenance cost, irrespective of the magnitude of the ODE errors and the model, CR3BP or ephemeris model. Contrary to targeting a 1.5 rev target horizon, other target horizons produced successful cases. The results from Davis et al.[11] and Guzzetti et al.[4] are analogous to this observation.

In the conventional x-axis control approach, once the maneuvers are executed at (or near) the apoapsis, the spacecraft is allowed to coast till the subsequent apoapsis where the next maneuver is generated and implemented. Since maneuvers induce a change in the state at the apoapsis, the effect of an implemented maneuver at the following apoapsis is vital. If the maneuver is implemented in the most stretching direction, the spacecraft experiences a larger deviation when it reaches the subsequent apoapsis and the phenomenon continues till the deviation is sufficiently magnified and the spacecraft is escaping. The flow defined by the Cauchy-Green tensor provides the magnitude and direction of the stretching, as available from the components of the monodromy matrix between two consecutive apoapses computed along a virtual reference orbit. The plot in Figure 9 summarizes the stretching as computed from the monodromy matrix for certain members of the NRHO family. For the orbit of interest, the 9:2 synodic L2 resonant orbit with perilune radius 3200 km, the three stretching directions are seen to possess magnitudes of stretching $\sigma_1 = 2.34$, $\sigma_2 = 0.78$ and $\sigma_3 = 0.25$. Since $\sigma_1 > 0$, the directions given by $\mathbb{V}_1$ and $\mathbb{U}_1$ correspond to direction of the perturbation growth at the initial and final times, respectively. On the contrary $\sigma_2, \sigma_3 < 1$, therefore directions $\mathbb{V}_2, \mathbb{V}_3$ at the initial time and $\mathbb{U}_2, \mathbb{U}_3$ at the final time are restoring directions where the magnitude of the perturbation diminishes over the propagated time. It is to be noted that the directions $\mathbb{V}_1, \mathbb{V}_2$ and $\mathbb{V}_3$ are perpendicular. For the L2 NRHO orbits with perilune radius between 2000-9000 km and with one maneuver per orbit, executed at the apoapsis, there exists a stretching direction and a restoring plane, thereby, ensuring maneuvers are perpendicular to the stretching direction that establishes the stability of the maneuvers.

The maneuver direction as compared to the stretching and restoring directions play an important role in determining the efficiency of the stationkeeping scheme. If successive maneuvers are implemented that are aligned closely to the $\mathbb{V}_1$ direction, the perturbations increase over time. On the contrary, any maneuvers aligned perpendicular to the $\mathbb{V}_1$ direction, in the restoring $\mathbb{V}_2 - \mathbb{V}_3$ plane, the perturbations do not grow sinificantly over the propagated time, hence, a better success rate for stationkeeping is achieved. When targeting different xz plane crossings near the periapsis region, i.e., downstream at 0.5 rev, 1.5 rev, and so on, a different maneuver direction, $\hat{M}$, is computed. The angle between the direction of the maneuver $\hat{M}$ and the most stretching direction of $\varphi_{C,v,v}$
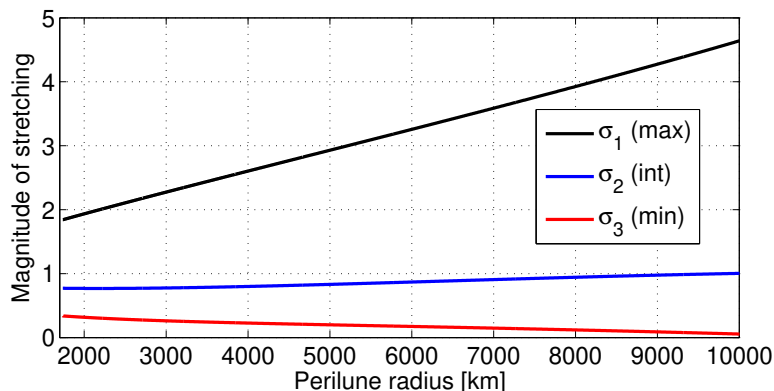

Figure 9: Magnitude of stretching σ_i along different $\mathbb{U}_i$ directions for various NRHOs in the L2 region.

for different target horizons, are summarized for an L2 NRHO with perilune radius 3200 km in Figure 10. A curve is also included for the angle between the direction of the maneuver $\hat{M}$ and the most stretching direction of $\varphi_{C,rv,v}$. Both these curves demonstrate a similar trend, but as noted previously, comparing with $\varphi_{C,v,v}$ is a good choice for halo orbits that are significantly sensitive to velocity perturbations. When targeting 1.5 revs ahead, the angle between the maneuver and the most stretching direction for $\varphi_{C,v,v}$ is approximately 50 degrees, while for the 6.5 rev target horizon the angle is nearly 90 degrees. For target horizons where the angle is almost perpendicular to the most stretching direction, i.e., aligned with the restoring plane, the state variations at the initial time do not induce a large final variation, hence, the spacecraft remains bounded closer to the reference trajectory. In contrast, at the 1.5 rev target horizon, the maneuver has a significant component in the most stretching direction that results in amplification of state variation at the final time for a specific initial state perturbation. In such a case, the deviation size and the maneuver size continuously increase with time and, eventually, divergence from the virtual reference trajectory occurs.

13

The maneuvers are based, of course, on the states along the actual trajectory nearby the baseline path and may not precisely align with the angles in Figure 10, therefore, the angle between the actual maneuvers as compared to the most stretching direction that result from Monte Carlo simulations are plotted in Figure 11 for both the CR3BP as well as the ephemeris model. For each of the target horizons, 0.5 rev, 1.5 rev and so on, the angle between the actual maneuvers and the most stretching direction $\mathbb{V}_1$ are well estimated in Figure 10. For the ephemeris case, due to the complex dynamics, the angles do not precisely coincide with the estimated values, but do follow

Figure 10: Angle between the maneuver and the most stretching directions for the 9:2 synodic resonant L2 NRHO with perilune radius 3200 km.

the underlying trend. The maneuvers as viewed in configuration space in Figure 12 for both the CR3BP and the ephemeris case, demonstrate distinctly different directions for the 1.5 rev target horizon and the 6.5 rev target horizon. Not surprisingly, a larger variance is observed for maneuvers in the ephemeris model as compared to the CR3BP model. In addition, the stretching direction as well as the restoring plane that are estimated using the underlying CR3BP dynamics are plotted in Figure 12(a), for the L2 NRHO with 3200 km perilune radius. Clearly, the direction of the maneuvers computed for different target horizons influences the performance of the stationkeeping algorithm. Not surprisingly, the characteristics of the flow along the orbit delivers a poor performance for the 1.5 rev target horizon, as the maneuvers have a significant component in the most stretching direction. In contrast, the 6.5 rev target horizon proves superior for the L2 NRHO with perilune radius 3200 km, as maneuvers are closely aligned with the restoring plane.
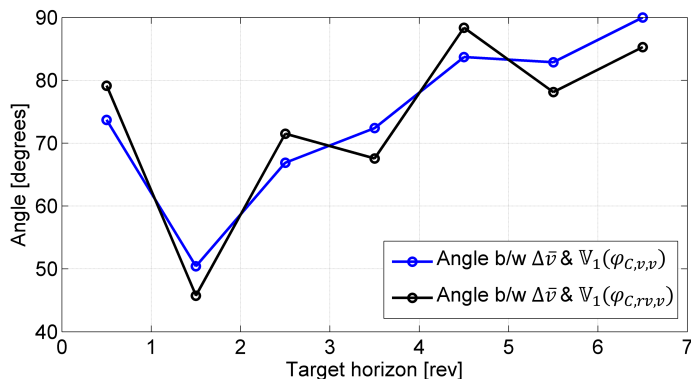
In the conventional x-axis control approach, the target condition determines the effectiveness of the maneuvers to maintain the spacecraft in the close vicinity of a virtual reference trajectory over time. The flow from the maneuver location to the target determines the direction and the magnitude of the maneuvers. As noted, although the maneuver magnitude depends on the initial error, the ratio of the maximum maneuver magnitude for an unit initial perturbation is deterministic in the linear sense. Similarly, the direction of the maneuver with respect to the most stretching direction is computable for any NRHO under investigation. The trend in maneuver magnitude and direction offers a control leverage metric, that evaluates the effectiveness of the maneuver and assists in an informative selection for the target horizon. The angle between the estimated maneuver and the most stretching direction appears in Figure 13(a). Clearly, for the range of NRHOs under investigation, the 1.5 rev target horizon is not recommended, as maneuvers possess a significant component in the most stretching direction that deviates away from the virtual reference trajectory over time. Depending on the orbit of interest, selecting 6.5 rev, 4.5 rev and 2.5 rev target horizons offer good performance. Targeting further downstream beyond 6.5 rev horizon is computationally intensive and does not necessarily yield any substantial improvements in stationkeeping costs. Other NRHOs, independently evaluated, may offer flow patterns that differ from the 9:2 synodic resonant NRHO in the L2 region, and different target horizons may yield different performance.

The x-axis approach is a loose control strategy that targets only two of the seven states (including time), i.e., the rotating $\dot{x}$ component at $y = 0$, thus providing low cost stationkeeping solutions. For different NRHOs, the annual orbit maintenance costs are computed for both low (3σ: 1 km and 1 cm/s) and high (3σ: 10 km and 10 cm/s) orbit determination error levels in Tables 1 and 2, respectively. For a particular orbit, irrespective of the orbit determination error levels, the annual stationkeeping costs generated by targeting relatively larger horizon times, i.e., 4.5, 5.5 and 6.5 revs, are not significantly different. For very low target horizon of 0.5 rev, significantly higher cost of operation is observed in contrast to targeting a longer time horizon. As noted earlier, no Monte Carlo runs yield successful maneuvers for a target horizon of 1.5 rev.

14
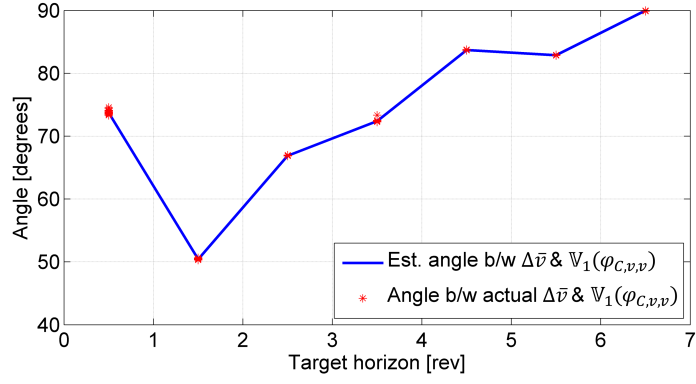
(a) CR3BP model
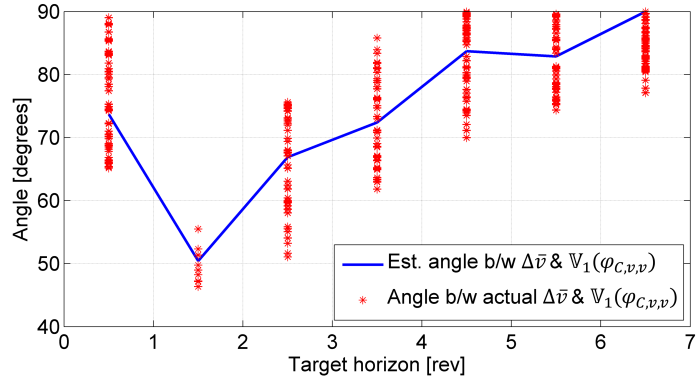
(b) Ephemeris model

Figure 11: Angle between the actual maneuver and the most stretching direction $\mathbb{V}_1(\varphi_{C,v,v})$ for the 9:2 synodic resonant L2 NRHO with perilune radius 3200 km. Low orbit determination error (3σ: 1 km and 1 cm/s) case.

Table 1: Annual orbit maintenance cost [m/s] with low orbit determination error level (3σ: 1 km and 1 cm/s).

Perilune radius [km]	Target horizon [rev]						
	0.5	1.5	2.5	3.5	4.5	5.5	6.5
3200	0.28	DNC	0.18	0.13	0.14	0.15	0.16
4000	0.29	DNC	0.18	0.13	0.14	0.15	0.15
4800	0.32	DNC	0.16	0.13	0.15	0.15	0.15
5645	0.45	DNC	0.16	0.13	0.15	0.14	0.15
6400	0.58	DNC	0.17	0.13	0.15	0.15	0.16
7200	0.72	DNC	0.18	0.13	0.16	0.15	0.15

* DNC - Did not converge

Phase control approach

Precise orbit control is expensive and may be nontrivial for spacecraft operations. The conventional x-axis control approach is effective in maintaining the spacecraft in the vicinity of a virtual reference solution at a low cost. By only targeting two of the seven states, the spacecraft remains loosely bounded in the neighborhood of the virtual reference path that is originally generated over a significantly longer duration. However, the low cost stationkeeping solutions generated by the conventional approach do not necessarily synchronize in phase space with the virtual reference trajectory, resulting in the actual trajectory lagging or leading the virtual reference in time space. Figure 14(a) illustrates the time difference between the actual trajectory and
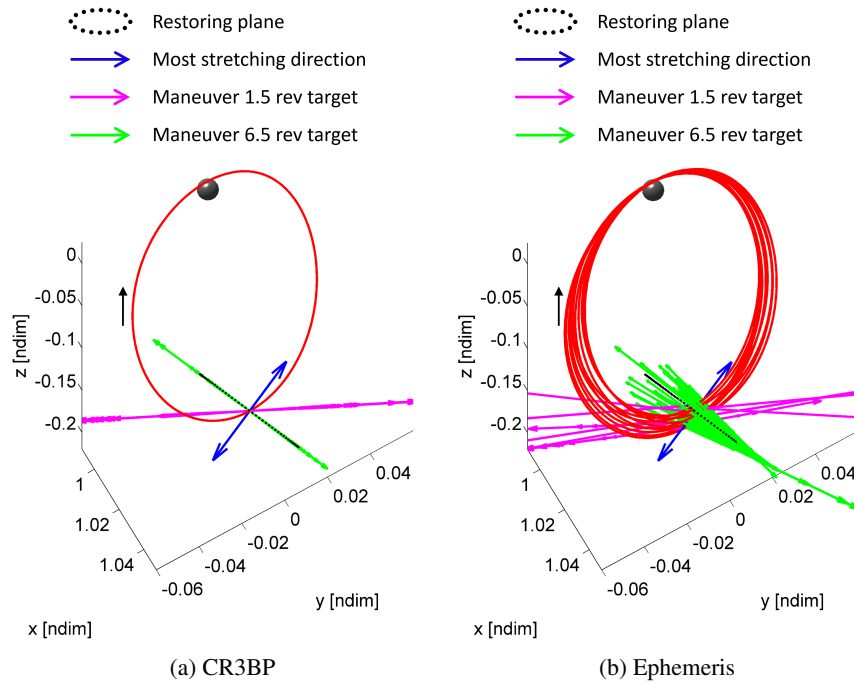
(a) CR3BP   (b) Ephemeris

Figure 12: Maneuvers in configuration space for L2 NRHO with perilune radius 3200 km.

Table 2: Annual orbit maintenance cost [m/s] with high orbit determination error level (3σ: 10 km and 10 cm/s).

| Perilune radius [km]	Target horizon [rev]						
	0.5	1.5	2.5	3.5	4.5	5.5	6.5
3200	5.84	DNC	1.81	1.02	0.96	0.90	0.91
4000	3.78	DNC	1.86	0.92	0.90	0.89	0.91
4800	3.73	DNC	1.58	0.93	0.86	0.85	0.82
5645	4.53	DNC	1.43	0.86	0.85	0.82	0.86
6400	7.16	DNC	1.42	0.88	0.80	0.81	0.83
7200	7.45	DNC	1.66	0.88	0.81	0.78	0.78

* DNC - Did not converge

the virtual reference measured at periapsis over different Monte Carlo runs, i.e., cases with different seeds for random errors to mimic an uncertainty in orbit determination. The phase difference between the actual trajectory and the virtual reference path increases either positively or negatively over time. If the baseline trajectory is generated to satisfy any eclipse avoidance properties or any other phase constraints, the phase shift between the actual and reference trajectories may impede the mission objectives. To overcome such a scenario, additional restrictions are imposed on the x-axis control algorithm to generate maneuvers that adhere to appropriate phasing of the actual trajectory. For controlling phase shift, Davis et al.[22] target the rotating $\dot{x}$ value as well as the periapsis altitude simultaneously. With the updated strategy a decrease in the rate of phase shift is observed. For any cases, where the spacecraft states have deviated significantly, a long horizon orbit correction maneuver is implemented to drive the states on to the virtual reference trajectory. An alternate approach with time shift feedback is explored.

To maintain the correct phasing between the actual trajectory and the virtual reference path, a phase constraint is delivered either at periapsis, or apoapsis, or even the xz-plane crossing, as they are complimentary. Since the x-axis control approach targets a condition at the xz-plane crossing, adding additional phase control constraints at the xz-plane crossing satisfies the requirement. A fixed time targeting scheme is incorporated
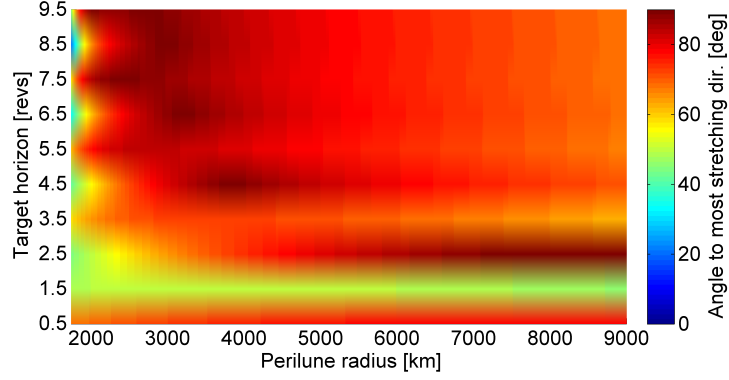
(a) Angle between the estimated maneuver and the most stretching direction
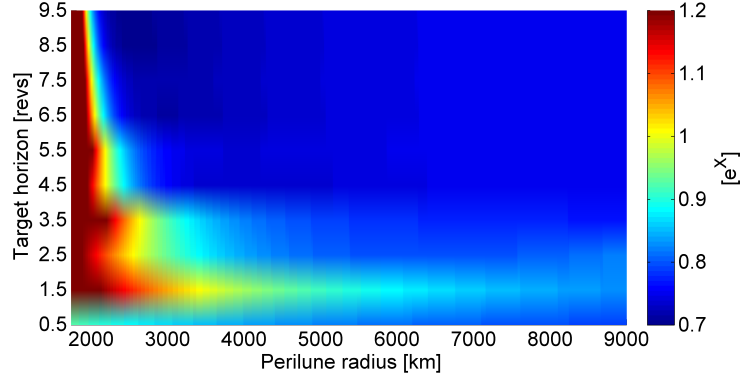
(b) Maximum maneuver magnitude per unit initial deviation (max value capped at 1.2)

**Figure 13**: Maneuver effectiveness for different target horizon over various NRHOs.

that targets conditions at the xz-plane crossing to occur at the same time relative to the virtual reference at the corresponding xz-plane crossing. A feedback constraint is formulated as

$$\Delta y_f - \dot{y}_f \Delta t_0 = \begin{bmatrix} \varphi_{T,24} & \varphi_{T,25} & \varphi_{T,26} \end{bmatrix} \Delta \bar{v}_0 \tag{12}$$

and solved along with the control equation as in equation (7) to compute the required maneuver. Here, the final time of propagation, $t_f = t_{Target} = t_{xz}^*$ is the time along the virtual reference trajectory at the appropriate xz plane crossing. The term $\dot{y}_f \Delta t_0$ in equation (12) is a feedback term to compensate for the adjustment in the phase difference detected at the apoapsis where the maneuver is executed. Additionally, Δy_f corresponds to the difference in y position between the actual and the reference trajectory at the end of the propagated trajectory. For a trajectory with no phase difference, $\Delta t_0 = 0$ and $\Delta y_f = 0$. With an iterative process, the states are updated to drive the left side of equation (12) to zero. The maneuver generated with an additional phase constraint bounds the spacecraft motion in the vicinity of the virtual reference trajectory in the time states as well.

Using a phase control approach, the phase shift between the actual trajectory and the virtual reference is minimized. Since the virtual reference is generated satisfying any eclipse or phase constraint, the actual trajectory also does not violate any phase constraint, to within a few seconds tolerance. Figure 14(b) demonstrates the efficacy of the phase control approach to minimize the time shift at periapsis for 100 Monte Carlo runs completed on the L2 NRHO with perilune radius 3200 km. The time difference, measured at the periapsis location is low, in contrast to Figure 14(a) using the conventional x-axis control approach.

The annual orbit maintenance cost for the stationkeeping with the phase control approach is higher than
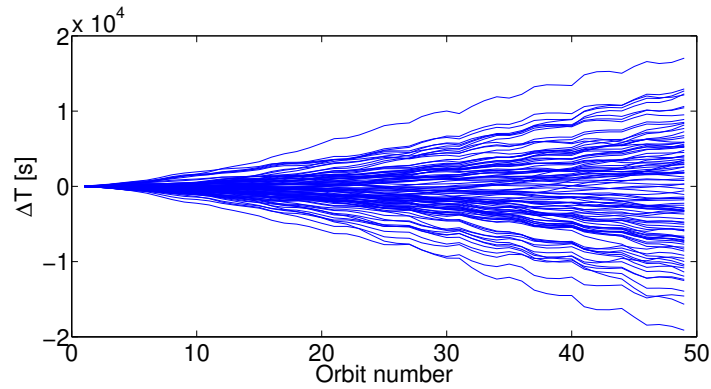
(a) Conventional approach
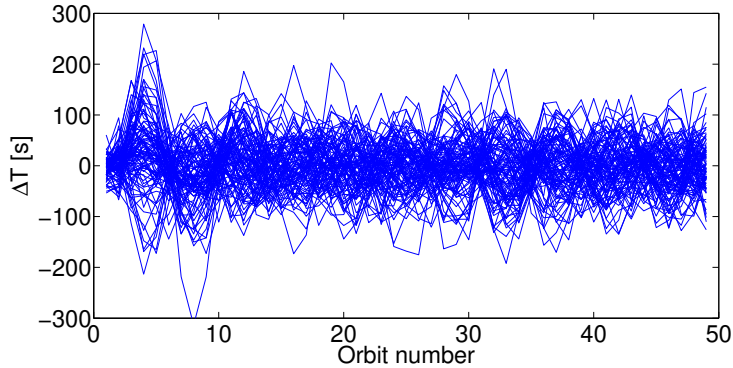
(b) Phase control approach

Figure 14: Phase shift measured at periapsis with and without phase control. L2 NRHO with perilune radius 3200 km.

the conventional approach. Not surprisingly, an additional constraint equation that is solved simultaneously with the control equation decreases the solution space and results in a higher cost of operations. The phase control approach works efficiently when the target horizon is sufficiently long. The approach produces favorable solutions for the 9:2 synodic resonant L2 NRHO when targeting 6.5 rev, 5.5 rev, 4.5 rev and 2.5 rev downstream. Although considerably better phasing than the conventional approach, diminishing returns are observed at 3.5 rev target horizon time. For short target horizons, i.e., 0.5 rev and 1.5 rev, the stiffer targeting conditions using phase control approach do not generate satisfactory results. Due to an additional constraint, an increase in the annual maintenance cost is detected. The costs for different NRHOs under consideration are listed in Tables 3 and 4 for low and high orbit determination errors, respectively. Marginal increases in costs are apparent as the perilune radius of the NRHOs increase.

CONCLUDING REMARKS

A stationkeeping technique using x-axis control is evaluated for low perilune radius NRHOs that offer candidate solutions for the Gateway mission. A systematic and straightforward approach is demonstrated that describes the interaction between the flow evolving from one maneuver location to the next during coast segments and the flow evolution from the maneuver location to the target, to identify the effectiveness of a generated maneuver. The convergence characteristics and the cost of operations using the conventional x-axis control approach is correlated to the flow along the corresponding reference orbit. For the L2 NRHOs with stationkeeping maneuvers only implemented at the apoapsis location, the maneuvers generated by targeting the rotating $\dot{x}$ value at the xz plane crossing 1.5 rev downstream yield maneuvers with a significant component in the stretching direction while the maneuver generated by targeting the xz plane crossing 6.5 rev

Table 3: Annual orbit maintenance cost [m/s] with low ODE level (3σ: 1 km and 1 cm/s) with phase constraints.

Perilune radius [km]	Target horizon [rev]						
	0.5	1.5	2.5	3.5	4.5	5.5	6.5
3200	DNC	DNC	0.24	0.33	0.26	0.30	0.31
4000	DNC	DNC	0.24	0.27	0.29	0.34	0.33
4800	DNC	DNC	0.23	0.27	0.33	0.37	0.34
5645	DNC	DNC	0.24	0.32	0.39	0.41	0.36
6400	DNC	DNC	0.26	0.42	0.51	0.50	0.39
7200	DNC	DNC	0.33	0.57	0.61	0.52	0.38

* DNC - Did not converge

Table 4: Annual orbit maintenance cost [m/s] with high ODE level (3σ: 10 km and 10 cm/s) with phase constraints.

Perilune radius [km]	Target horizon [rev]						
	0.5	1.5	2.5	3.5	4.5	5.5	6.5
3200	DNC	DNC	2.02	2.51	1.98	2.28	2.62
4000	DNC	DNC	1.91	2.00	2.06	2.23	2.13
4800	DNC	DNC	1.80	1.89	2.03	2.31	2.09
5645	DNC	DNC	1.77	2.08	2.19	2.33	1.99
6400	DNC	DNC	1.79	2.46	2.49	2.31	2.09
7200	DNC	DNC	1.85	2.84	2.74	2.47	2.14

* DNC - Did not converge

downstream generates maneuvers aligned in the restoring directions resulting in efficient maneuver characteristics and lower orbit maintenance costs.

The low stationkeeping costs generated by the x-axis control approach is a result of a loose requirement for boundedness around a virtual reference solution, and appropriate in various mission scenarios. The absence of an active phase control, however, causes the actual trajectory to shift in phase from the virtual reference solution. When a tight phase control is required to satisfy mission constraints such as eclipse avoidance, a feedback phase constraint is introduced along with targeting the rotating $\dot{x}$ value to compute a maneuver. Such a strategy maintains tight phasing between the actual and the virtual reference over long duration.

REFERENCES

[1] M. Mammarella, C. A. Paissoni, N. Viola, R. Fusaro, and T. Andrenussi, "High-Power Electric Propulsion Enabling Support to the future Deep Space Gateway," *2018 AIAA SPACE and Astronautics Forum and Exposition*, 2018, p. 5189.

[2] J. C. Crusan, R. M. Smith, D. A. Craig, J. M. Caram, J. Guidi, M. Gates, J. M. Krezel, and N. B. Herrmann, "Deep space gateway concept: Extending human presence into cislunar space," *2018 IEEE Aerospace Conference*, IEEE, 2018, pp. 1–10.

[3] E. M. Zimovan, K. C. Howell, and D. C. Davis, "Near rectilinear halo orbits and their application in cislunar space," *3rd IAA Conference on Dynamics and Control of Space Systems, Moscow, Russia*, 2017, p. 20.

[4] D. Guzzetti, E. M. Zimovan, K. C. Howell, and D. C. Davis, "Stationkeeping analysis for spacecraft in lunar near rectilinear halo orbits," *27th AAS/AIAA Space Flight Mechanics Meeting*, AAS Marriott Plaza, Texas, 2017, pp. 1–20.

[5] W. Wu, Y. Tang, L. Zhang, and D. Qiao, "Design of communication relay mission for supporting lunar-farside soft landing," *Science China Information Sciences*, Vol. 61, No. 4, 2018, p. 040305.

[6] M. Lemelin, D. M. Blair, C. E. Roberts, K. D. Runyon, D. Nowka, and D. A. Kring, "High-priority lunar landing sites for in situ and sample return studies of polar volatiles," *Planetary and Space Science*, Vol. 101, 2014, pp. 149–161.

[7] L. Bucci, M. Lavagna, and R. Jehn, "Station keeping techniques for near rectilinear orbits in the Earth–Moon system," *Proceedings of 10th international ESA conference on GNC systems, Salzburg, Austria*, Vol. 29, 2017.

[8] G. Gómez, K. Howell, J. Masdemont, and C. Simó, "Station-keeping strategies for translunar libration point orbits," *Advances in Astronautical Sciences*, Vol. 99, No. 2, 1998, pp. 949–967.

[9] K. C. Howell and T. M. Keeter, "Station-keeping strategies for libration point orbits- Target point and Floquet Mode approaches," *Spaceflight mechanics 1995*, 1995, pp. 1377–1396.

[10] V. Muralidharan, "Orbit Maintenance Strategies for Sun-Earth/Moon Libration Point Missions: Parameter Selection for Target Point and Cauchy-Green Tensor Approaches," M.S. Thesis, Purdue University, 2017.

[11] D. C. Davis, S. M. Phillips, K. C. Howell, S. Vutukuri, and B. P. McCarthy, "Stationkeeping and transfer trajectory design for spacecraft in cislunar space," *AAS/AIAA Astrodynamics Specialist Conference*, 2017.

[12] D. Davis, S. Bhatt, K. Howell, J.-W. Jang, R. Whitley, F. Clark, D. Guzzetti, E. Zimovan, and G. Barton, "Orbit maintenance and navigation of human spacecraft at cislunar near rectilinear halo orbits," *AIAA Space Flight Mechanics Meeting, AAS*, 2017.

[13] D. Folta and F. Vaughn, "A Survey of Earth-Moon Libration Orbits: Stationkeeping Strategies and Intra-Orbit Transfers," *AIAA/AAS Astrodynamics Specialist Conference and Exhibit*, 2004, p. 4741.

[14] D. Folta, T. Pavlak, K. Howell, M. Woodard, and D. Woodfork, "Stationkeeping of Lissajous trajectories in the Earth-Moon system with applications to ARTEMIS," *AIAA/AAS Astrodynamics Specialist Conference*, 2010.

[15] V. Szebehely, "Theory of orbits: the restricted problem of three bodies," tech. rep., Yale univ New Haven CT, 1967.

[16] K. C. Howell, "Three-dimensional, periodic,'halo'orbits," *Celestial mechanics*, Vol. 32, No. 1, 1984, pp. 53–71.

[17] C. Acton, N. Bachman, J. Diaz Del Rio, B. Semenov, E. Wright, and Y. Yamamoto, "Spice: A means for determining observation geometry," *EPSC–DPS Joint Meeting*, 2011.

[18] T. Pavlak and K. Howell, "Strategy for optimal, long-term stationkeeping of libration point orbits in the Earth-Moon system," *AIAA/AAS Astrodynamics Specialist Conference*, 2012, p. 4665.

[19] V. Muralidharan, A. Weiss, and U. V. Kalabic, "Control Strategy for Long-Term Station-Keeping on Near-Rectilinear Halo Orbits," *AIAA Scitech 2020 Forum*, 2020, p. 1459.

[20] M. Shirobokov, S. Trofimov, and M. Ovchinnikov, "Survey of station-keeping techniques for libration point orbits," *Journal of Guidance, Control, and Dynamics*, Vol. 40, No. 5, 2017, pp. 1085–1105.

[21] D. C. Folta, T. A. Pavlak, A. F. Haapala, K. C. Howell, and M. A. Woodard, "Earth–Moon libration point orbit stationkeeping: theory, modeling, and operations," *Acta Astronautica*, Vol. 94, No. 1, 2014, pp. 421–433.

[22] D. C. Davis, F. S. Khoury, K. C. Howell, and D. J. Sweeney, "Phase Control and Eclipse Avoidance in Near Rectilinear Halo Orbits," *43rd AAS Guidance, Navigation and Control Conference, Breckenridge, CO, United States*, 2020.

[23] K. C. Howell and S. C. Gordon, "Orbit determination error analysis and a station-keeping strategy for Sun-Earth L1 libration point orbits," *Journal of the Astronautical Sciences*, Vol. 42, 1994, pp. 207–228.

[24] R. L. Anderson, M. W. Lo, and G. H. Born, "Application of local Lyapunov exponents to maneuver design and navigation in the three-body problem," *AIAA/AAS Astrodynamics Specialist Conference*, 2003.

[25] G. Haller, "Lagrangian coherent structures from approximate velocity data," *Physics of fluids*, Vol. 14, No. 6, 2002, pp. 1851–1861.

[26] C. R. Short and K. C. Howell, "Lagrangian coherent structures in various map representations for application to multi-body gravitational regimes," *Acta Astronautica*, Vol. 94, No. 2, 2014, pp. 592–607.

[27] J. S. Subirana, J. J. Zornoza, and M. Hernández-Pajares, "Gnss data processing. volume 1: Fundamentals and algorithms," *ESA Communications ESTEC, PO Box*, Vol. 299, 2013, p. 2200.